Design and Analysis of a Blind Juggling Robot

Philipp Reist, *Student Member, IEEE*, and Raffaello D'Andrea, *Fellow, IEEE*

***Abstract*—We present the design of the Blind Juggler: a robot that is able to juggle an unconstrained ball without feedback at heights of up to 2 m. The robot actuates a parabolic aluminum paddle with a linear motor. We achieve open-loop stability of the ball trajectory with two design parameters: 1) the curvature of the parabolic paddle and 2) the acceleration of the paddle at impact. We derive a linear map of perturbations of the nominal ball trajectory over a single bounce and obtain local stability of the trajectory by tuning the eigenvalues of this mapping with the two design parameters. We consider nine ball states in this analysis, including ball spin. Experimental data provide the impact states of the ball and paddle. From these data, we can identify system parameters and infer the process noise introduced into the system. We then combine the experimental noise power spectral densities with a model of the system and optimize the design parameters such that the impact of the process noise on juggling performance is minimized. Theoretical as well as experimental results of the optimization are discussed.**

***Index Terms*—Bouncing ball, dexterous manipulation, dynamics, juggling, mechanism design.**

I. Introduction

THE Blind Juggler, which is shown in Fig. 1, demonstrates that high-performance robotic juggling of unconstrained balls is possible without using sensors. The Blind Juggler can juggle at apex heights of up to 2 m, even though the robot cannot tilt or pan the aluminum paddle, which is actuated by a linear motor. In effect, the Blind Juggler can stabilize a ball in three dimensions with only a single actuated degree of freedom. Since there is no feedback, we achieve open-loop stability of the ball trajectory using two key design elements: 1) The paddle has a slightly concave, parabolic shape, which keeps the ball from bouncing off the robot; and 2) a decelerating striking motion of the paddle stabilizes the apex height of the ball. In experiments, the Blind Juggler is able to continuously juggle a variety of balls at different heights, and exhibits substantial robustness to horizontal and vertical perturbations.

In particular, the two key design parameters are the curvature of the parabolic paddle shape and the acceleration of the paddle at ball impact. We determine the specific values of the design parameters by analyzing the local stability of the nominal ball trajectory. Using a model of the ball dynamics, we perform a perturbation analysis of the trajectory and calculate how perturbations introduced at the apex map to the next apex. We consider nine ball states in this analysis: all translational positions and velocities, and ball spin. Using first-order approximations to the system dynamics, we obtain a linear map, i.e., a linearized Poincaré map of the perturbations over a single bounce. We tune the eigenvalues of this mapping with the paddle curvature and acceleration to achieve local stability for a range of apex heights and ball parameters.

Fig. 1. The Blind Juggler bouncing a superball. The user interface features two buttons to control the juggling height.

We use a video camera and a microphone to measure impact states of the ball and paddle in order to assess juggling performance in terms of impact location and apex height variance. We also use these measurements to identify system parameters, such as the ball coefficient of restitution, and to infer the process noise introduced into the system by imperfect paddle motions and stochastic ball impact properties.

We use the process noise measurements to refine the design parameters and improve juggling performance. First, we set up a linear, time-invariant system that models how the noise input maps to the outputs: the deviations in ball impact location and apex height. These outputs are what we want to keep small.

Manuscript received September 15, 2011; revised February 8, 2012; accepted June 15, 2012. Date of publication July 30, 2012; date of current version December 3, 2012. This paper was recommended for publication by Associate Editor A. Albu-Schäffer and Editor W. K. Chung upon evaluation of the reviewers' comments.

The authors are with the Institute for Dynamic Systems and Control, ETH Zurich, CH-8092 Zurich, Switzerland (e-mail: reistp@ethz.ch; rdandrea@ethz.ch).

This paper has supplementary downloadable material available at http://ieeexplore.ieee.org.

Digital Object Identifier 10.1109/TRO.2012.2205493

Next, we use the frequency response of the linear system together with the experimental power spectral densities (PSDs) of the process noise to calculate the output variance as a function of the design parameters. We, then, find the design parameters that minimize the output variance. Theoretical results predict a performance improvement for the apex height and no improvement for the impact location. This is also confirmed in experiments. The small impact of the paddle curvature on the impact location variance allows us to choose the curvature according to secondary criteria such as, for example, maximal achievable apex height.

This paper is structured as follows: After an overview of related work, we derive the nominal ball trajectory in Section II. The perturbation analysis is presented in Section III. We find stabilizing design parameters in Section IV. The prototype of the Blind Juggler and experimental results are discussed in Section V. Finally, we optimize the design parameters and discuss theoretical and experimental results in Section VI.

A. Related Work

This paper is based on previous work published in [1], where we presented preliminary results obtained with a prototype of the Blind Juggler. New contributions compared with previous work include the stability analysis for nine ball states (previously a planar model) and using measured noise PSDs for the design parameter optimization (previously assumed white process noise).

The bouncing ball system has received attention in dynamics, as it is a simple system that exhibits rich dynamical behavior, i.e., period doubling (bifurcations) leading to chaos [2], [3]. Holmes showed that even with energy dissipation present in the form of a coefficient of restitution, chaotic motions of the ball result for sufficiently high excitation levels [2]. Vincent presented a control strategy for bouncing a ball at a fixed height that exploits chaotic behavior [4].

In robotics, juggling is considered a challenging dexterous task. Buehler *et al.* were amongst the first to study robotic juggling using a planar juggling robot [5]. The robot consists of a rotating bar equipped with a billiard cushion batting a puck on an inclined table. Using position feedback, the robot is able to simultaneously juggle up to two pucks. It uses a feedback strategy called the mirror law introduced by Buehler *et al.* [6], [7]. The algorithm defines the trajectory of the paddle as a mirrored (about the desired impact height) and scaled version of the ball's trajectory. Consequently, this requires constant tracking of the ball's position. The mirror law produces paddle trajectories that accelerate at impact, which contrasts with the results presented in this paper, and with results obtained by Schaal and Atkeson, who analyzed the apex height stabilizing property of a decelerating paddle for an open-loop bouncing ball system [8]. An interesting aside is that Schaal *et al.* found that a decelerating striking motion is a strategy intuitively used by humans when trying to bounce a ball at a fixed height on a racket [9]. The related task of dribbling a basketball with a robot arm using force or vision feedback was explored by Baetz *et al.* [10]. In legged robotics, a hopping robot is similar to a bouncing ball system. Ringrose presented the design of a self-stabilizing monopod featuring a curved foot in [11], which is similar to sensorless bouncing of a ball on a parabolic paddle.

Robotic juggling has motivated the development of advanced control methods such as Burridge's work on juggling an unconstrained ball in the presence of obstacles using a cascade of controllers [12]. This control strategy, which uses vision feedback, was evaluated on a direct drive robot arm, the Bühgler. With the same arm, Rizzi *et al.* extended the mirror law to unconstrained balls and achieved simultaneous juggling of two balls [13]. Kulchenko and Todorov developed a model predictive control strategy for juggling up to two unconstrained table tennis balls with a single racket using a haptic robot [14]. Other work on control involving juggling robots includes Sanfelice's hybrid control strategies to stabilize juggling of multiple balls [15] and Zavala–Río's method that deals with uncertainty in the coefficient of restitution [16]. Schaal and Atkeson used a juggling setup to develop robot learning strategies, where a robot arm iteratively learns to juggle a ball on a plate [17]. Sakaguchi *et al.* also studied learning strategies using a planar robot arm that juggles bean bags by throwing and catching [18].

Related to the concepts presented here is the work by Ronsse *et al.*, who analyzed different juggling systems [19]–[22], and introduced the term "blind" juggling robot in [22], where they presented a planar ball-in-wedge juggling robot that is able to juggle purely feed forward or with feedback using measured impact times. Their robot is even able to generate a juggling pattern similar to the shower pattern, where the balls follow a circular path. In [21] and [22], Ronsse *et al.* addressed robustness of the bouncing ball system to static and dynamic errors in the ball's coefficient of restitution. The authors first derived the transfer function of the errors to the postimpact velocity perturbations. Then, they placed the zero of the transfer function by adjusting the paddle acceleration to either compensate for static or dynamic errors. This is an alternative strategy to the parameter optimization we present in this paper. Hobbelen and Wisse presented an H_2-norm inspired gait sensitivity norm that can be used to determine disturbance rejection capabilities of limit cycle walking robots [23]. The authors further showed that a stability measure, such as the spectral radius of a linearized Poincaré map, is a poor indicator of actual system performance in the presence of stochastic disturbances. They proposed their H_2-norm inspired performance metric as a better indicator. The gait sensitivity norm [24] can serve as a guide for design parameter selection for a walking robot, which is similar to the variance optimization we present in this paper. Mombaur *et al.* used optimization to find stabilizing design parameters for open-loop walking robots in [25]. The authors used the spectral radius of the linearized Poincaré map as the objective function to minimize in order to find design parameters resulting in a spectral radius smaller than one, which implies stability.

The Blind Juggler is able to juggle unconstrained balls without sensing. In the literature, many robots are studied that juggle constrained balls. Examples include the single degree-of-freedom bouncing ball setup by Vincent [4] or the planar juggling robots analyzed by Buehler [5] and Ronsse *et al.* [22]. Robots juggling unconstrained balls in three dimensions

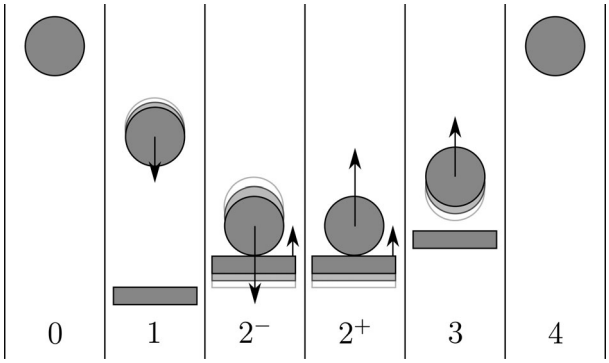

Fig. 2. Nominal ball trajectory. The ball starts at rest at the apex, 0. It is then subject to free fall, 1, before it impacts with the paddle, 2^-. After impact 2^+, the ball is again subject to free fall, 3, until it reaches again the apex, 4, which is identical to the initial apex, 0.

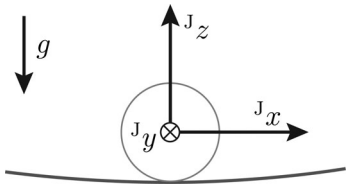

Fig. 3. Definition of the coordinate system J. The sketched ball and paddle are at nominal impact positions. The origin of J is fixed at the center of the ball at nominal impact position, and the z-axis is aligned with gravity g.

typically feature a robotic arm; the robot used by Rizzi *et al.* in [13] is one such example. These more complex robots use cameras to continuously track the ball's position. Schaal and Atkeson presented an open-loop juggling robot that features a paddle that passively keeps the ball in its center: they used a trampoline-like racket to stabilize the horizontal degrees of freedom of the ball [8]. Their focus, however, was on the analysis of the vertical stability of the ball.

II. Nominal Ball Trajectory

We introduce the nominal ball trajectory, which is sketched in Fig. 2. In the stability analysis, we consider the ball state $S := (x, \dot{x}, \omega_y, y, \dot{y}, \omega_x, z, \dot{z}, \omega_z)^\mathsf{T}$, where $^\mathsf{T}$ denotes the transpose. All elements are defined in the coordinate system J shown in Fig. 3. The positions $x, y,$ and z describe the location of the center of the ball. The ball velocities are $\dot{x}, \dot{y},$ and $\dot{z}$, and the ball spins $\omega_x, \omega_y,$ and ω_z are defined by the right-hand rule. We choose the particular grouping of the states since the spin ω_y interacts with the horizontal velocity $\dot{x}$ at impact, and ω_x with $\dot{y}$.

Nominally, all states except z and $\dot{z}$ are zero. However, because we use the full nominal ball states in the perturbation analysis in the next section, we derive them in the following.

A. Initial Apex

The ball starts at time $t = 0$ at the nominal apex height $z(0) = H$. Its state is

$$\bar{S}_0 = (0, 0, 0, 0, 0, 0, H, 0, 0)^\mathsf{T} \tag{1}$$

where the subscript 0 denotes the initial apex, and an overbar denotes a nominal state.

B. Free Fall

Next, the ball is in free fall. We ignore aerodynamic drag and obtain the differential equation

$$\ddot{z}(t) = -g \tag{2}$$

where $g = 9.81$ m/s^2 is the gravitational acceleration. Given initial conditions z_0 and $\dot{z}_0$ at $t = 0$, its solution is

$$z(t) = -\frac{g}{2}t^2 + \dot{z}_0 t + z_0 \tag{3}$$

$$\dot{z}(t) = -gt + \dot{z}_0. \tag{4}$$

The nominal initial conditions are $\dot{\bar{z}}_0 = 0$ and $\bar{z}_0 = H$. The free fall ends at impact with the paddle, which is at $z(T) = 0$ (see Fig. 3). The nominal impact time is

$$T = \sqrt{\frac{2H}{g}} \tag{5}$$

and the nominal ball impact velocity is

$$\dot{\bar{z}}_1 = -gT. \tag{6}$$

The ball state at $t = T$ is denoted with the subscript 1. The nominal state is

$$\bar{S}_1 = (0, 0, 0, 0, 0, 0, 0, \dot{\bar{z}}_1, 0)^\mathsf{T}. \tag{7}$$

Nominally, $\bar{S}_1$ and the preimpact $(-)$ ball state are identical $\bar{S}_2^- = \bar{S}_1$. We still introduce two separate nominal states since in the perturbation analysis, the perturbed states at the nominal impact time and at the actual impact time differ.

C. Impact

Nominally, the vertical ball velocity is inverted at impact such that the initial apex height is reached again. The postimpact $(+)$ ball state is therefore

$$\bar{S}_2^+ = (0, 0, 0, 0, 0, 0, 0, -\dot{\bar{z}}_1, 0)^\mathsf{T}. \tag{8}$$

We further derive the nominal paddle state at impact. The paddle state is $P = (z_\mathrm{P}, \dot{z}_\mathrm{P})^\mathsf{T}$, since the paddle has only a single translational degree of freedom. The state is defined in the coordinate system J, and z_P captures the height of the center of the paddle surface. At impact, the ball is in contact with the paddle (see Fig. 3), and the nominal paddle state is therefore

$$\bar{P}_2 = \bar{P}_1 = (-R, \dot{\bar{z}}_{\mathrm{P}1})^\mathsf{T} \tag{9}$$

where R is the ball radius and the nominal paddle velocity $\dot{\bar{z}}_{\mathrm{P}1}$ is obtained using Newton's impact law

$$\dot{z}^+ = -e_z \dot{z}^- + (1 + e_z)\dot{z}_\mathrm{P} \tag{10}$$

where $\dot{z}^-$ and $\dot{z}^+$ are the pre- and postimpact ball velocities, respectively. Damping losses at impact are modeled by the vertical coefficient of restitution $e_z \in [0, 1]$. In (10), we assume that the ratio of the ball mass to the paddle mass is small enough for the change in paddle impulse to be negligible (this ratio is

$\approx 3 \times 10^{-4}$ for the Blind Juggler). For this reason, we do not distinguish between the pre- and postimpact paddle state and omit the superscripts $(+,-)$. With (7) and (8) in (10), we find

$$\dot{\tilde{z}}_{\mathrm{P}1} = -\dot{\tilde{z}}_1 \frac{1-e_z}{1+e_z}. \tag{11}$$

D. Free Fall After Impact and Apex

After impact, the ball is in free fall until it reaches the nominal apex height again. The duration of the second free fall is identical to the first, resulting in the final apex time $t = 2T$. Nominally, the state after free fall (subscript 3), the state at final apex time (subscript 4), and the initial apex state are all identical

$$\bar{S}_3 = \bar{S}_4 = \bar{S}_0. \tag{12}$$

We introduce $\bar{S}_3$ because, in the perturbation analysis, the perturbed ball states after free fall and at nominal apex time are not identical.

III. Perturbation Analysis

In the following, we derive how perturbations, which are added to the nominal ball apex state, map over a single bounce to the next apex, i.e., from 0 to 4 in Fig. 2. We assume that the perturbations are small and use first-order approximations to the system dynamics. Experimental data presented in Section V show that the perturbations are indeed small. Therefore, the actual nonlinear system dynamics are captured well by a first-order model. In the following analysis, we derive the matrices that describe the first-order perturbation dynamics of each part of the trajectory illustrated in Fig. 2. These matrices form the basis for the results presented in the rest of this paper. The matrices show that to first order, the ball perturbation dynamics in x, y, and z are mutually decoupled; they can be used to analyze the local stability of the ball trajectory; and finally, we use them in the design parameter optimization.

A Mathematica notebook with the following analysis is included in the multimedia files provided with this paper.

A. Introduce Perturbations

The perturbed ball apex state is

$$S_0 = \bar{S}_0 + s_0 \tag{13}$$

where the elements of the initial perturbations are

$$s_0 := \left(s_{x0}, s_{\dot{x}0}, s_{\omega_y 0}, s_{y0}, s_{\dot{y}0}, s_{\omega_x 0}, s_{z0}, s_{\dot{z}0}, s_{\omega_z 0}\right)^{\mathsf{T}}. \tag{14}$$

B. Free Fall

We derive the mapping of the perturbations from apex, $t = 0$, to the nominal impact time $t = T$. First, we calculate the full state trajectory. The vertical ball trajectory is already established with (3) and (4). Without aerodynamic drag, the horizontal and spin dynamics are

$$\ddot{x} = \ddot{y} = 0 \tag{15}$$

$$\dot{\omega}_x = \dot{\omega}_y = \dot{\omega}_z = 0. \tag{16}$$

Given initial conditions $x_0, \dot{x}_0, \omega_{y0}, y_0, \dot{y}_0, \omega_{x0}$, and ω_{z0}, the solution is

$$x(t) = x_0 + \dot{x}_0 t, \qquad y(t) = y_0 + \dot{y}_0 t \tag{17}$$

$$\dot{x}(t) = \dot{x}_0, \qquad \dot{y}(t) = \dot{y}_0 \tag{18}$$

$$\omega_y(t) = \omega_y, \qquad \omega_x(t) = \omega_{x0} \tag{19}$$

$$\omega_z(t) = \omega_{z0}. \tag{20}$$

Inspecting the previous and the vertical trajectories (3), (4), we find that they are all linear in the initial conditions. Therefore, the perturbed ball state at nominal impact time T is exactly

$$S_1 = \bar{S}_1 + s_1 \tag{21}$$

$$s_1 = \mathrm{M}_{10} s_0. \tag{22}$$

The matrix M_{10} is the exact mapping of the initial perturbations s_0 to the perturbations s_1 at nominal impact time, and is block diagonal

$$\mathrm{M}_{10} = \begin{bmatrix} \mathrm{N}_{10} & 0 & 0 \\ 0 & \mathrm{N}_{10} & 0 \\ 0 & 0 & \mathrm{N}_{10} \end{bmatrix}, \quad \mathrm{N}_{10} = \begin{bmatrix} 1 & T & 0 \\ 0 & 1 & 0 \\ 0 & 0 & 1 \end{bmatrix}. \tag{23}$$

C. Impact

We derive the perturbation mapping over the impact in two steps. First, we calculate the deviation from nominal impact time, which is caused by the ball perturbations. Second, we calculate how the perturbations map over the impact.

1) Impact Time: Due to the perturbations, the impact occurs at the perturbed impact time $T + \tau$. The horizontal ball states are irrelevant for the calculation of τ, since to first order in x and y, the parabolic paddle is flat in its center.

We first approximate the vertical ball and paddle trajectory to first order. Using the perturbed ball state at nominal impact time S_1 (21) as new initial condition in the vertical ball trajectory (3), we find

$$\tilde{z}(\tau) = s_{z1} + (\dot{\tilde{z}}_1 + s_{\dot{z}1})\,\tau - \frac{g}{2}\tau^2 \tag{24}$$

where s_{z1} and $s_{\dot{z}1}$ are the perturbations in ball height and vertical velocity at nominal impact time, respectively. To first order in the time and state perturbations, the trajectory is therefore

$$z(\tau) = s_{z1} + \dot{\tilde{z}}_1 \tau. \tag{25}$$

Next, we derive the paddle trajectory. The paddle dynamics are

$$\ddot{z}_{\mathrm{P}}(\tau) = a_{\mathrm{P}} \tag{26}$$

where a_{P} is the constant paddle acceleration at impact, which is one of the two key design parameters. Using the nominal paddle impact state $\bar{P}_1$ (9) as initial condition, the solution is analogous to (24). Therefore, to first order

$$z_{\mathrm{P}}(\tau) = -R + \dot{\tilde{z}}_{\mathrm{P}1} \tau \tag{27}$$

where R is the ball radius. The impact occurs when the ball is in contact with the paddle

$$z(\tau) - z_{\mathrm{P}}(\tau) = R. \tag{28}$$

We solve for τ and obtain

$$\tau = \frac{s_{z1}}{\dot{\bar{z}}_{\mathrm{P}1} - \dot{\bar{z}}_1}. \tag{29}$$

Note that $\dot{\bar{z}}_1$ is strictly negative and $\dot{\bar{z}}_{\mathrm{P}1}$ is strictly positive; therefore, the denominator is always $\neq 0$ and τ is well defined. We rewrite (29) in matrix form

$$\tau = \mathrm{M}_{\tau 1} s_1 \tag{30}$$

$$\mathrm{M}_{\tau 1} = \begin{bmatrix} 0 & 0 & 0 & 0 & 0 & 0 & \dfrac{1}{\dot{\bar{z}}_{\mathrm{P}1} - \dot{\bar{z}}_1} & 0 & 0 \end{bmatrix}. \tag{31}$$

Next, we derive what the ball and paddle perturbations are at actual impact time, $T + \tau$. To first order, the perturbed ball and paddle states at impact are

$$S_2^- = S_1 + \dot{\bar{S}}_1 \tau \tag{32}$$

$$= \bar{S}_1 + s_1 + \dot{\bar{S}}_1 \mathrm{M}_{\tau 1} s_1 \tag{33}$$

$$P_2 = \bar{P}_1 + \dot{\bar{P}}_1 \tau \tag{34}$$

$$= \bar{P}_1 + \dot{\bar{P}}_1 \mathrm{M}_{\tau 1} s_1 \tag{35}$$

where we use the nominal time derivative of the impact states

$$\dot{\bar{S}}_1 = (0, 0, 0, 0, 0, 0, \dot{\bar{z}}_1, -g, 0)^{\mathsf{T}} \tag{36}$$

$$\dot{\bar{P}}_1 = (\dot{\bar{z}}_{\mathrm{P}1}, a_{\mathrm{P}})^{\mathsf{T}} \tag{37}$$

and that to first order $\dot{S}_1 \tau = \dot{\bar{S}}_1 \tau$. Finally, the ball and paddle preimpact $(-)$ perturbations are

$$s_2^- = s_1 + \dot{\bar{S}}_1 \mathrm{M}_{\tau 1} s_1 = \left(\mathrm{I} + \dot{\bar{S}}_1 \mathrm{M}_{\tau 1} \right) s_1 \tag{38}$$

$$p_2 = \dot{\bar{P}}_1 \mathrm{M}_{\tau 1} s_1 \tag{39}$$

where I is the identity matrix.

With the ball and paddle states defined at actual impact, we proceed to the perturbation mapping over the impact. We introduce the necessary coordinate transformations and then apply the impact function to the transformed paddle and ball states. Finally, we calculate, to first order, how the perturbations are mapped to the postimpact ball state.

2) Impact Velocities: The impact affects only the ball velocities. In order to simplify the following derivation, we define a velocity state for the ball

$$V_{\mathrm{S}} := (\dot{x}, \dot{y}, \dot{z}, \omega_x, \omega_y, \omega_z)^{\mathsf{T}} = \mathrm{T}_{\mathrm{VS}} S \tag{40}$$

where T_{VS} is the straightforward transformation matrix. Analogously for the paddle, we only consider its vertical velocity

$$\dot{z}_{\mathrm{P}} = \mathrm{T}_{\mathrm{VP}} P, \quad \mathrm{T}_{\mathrm{VP}} = \begin{bmatrix} 0 & 1 \end{bmatrix}. \tag{41}$$

3) Impact Coordinate System: The horizontal impact model, which is introduced later, acts on velocities and spins that are tangential and perpendicular to the impact surface. Due to the perturbations, the ball impact is off-center. The impact surface is defined by the parabolic paddle surface which satisfies

$$z = \frac{c}{2} \left({}^{\mathrm{J}}x^2 + {}^{\mathrm{J}}y^2 \right) = \frac{c}{2} r^2 \tag{42}$$

where r is the radial distance from the paddle center, and c is the paddle curvature, which is the other key design parameter besides the paddle acceleration a_{P}. We derive the coordinate transformations in order to express the velocity states V_{S} and $\dot{z}_{\mathrm{P}}$ in the impact coordinate system C (see Fig. 4). In the following, we use preceding superscripts to denote the coordinate system a vector or coordinate is expressed in. For example, ${}^{\mathrm{C}}V_{\mathrm{S}}$ is the ball velocity expressed in coordinate system C. All states and coordinates without a coordinate system superscript are by default expressed in the coordinate system J, defined in Fig. 3.

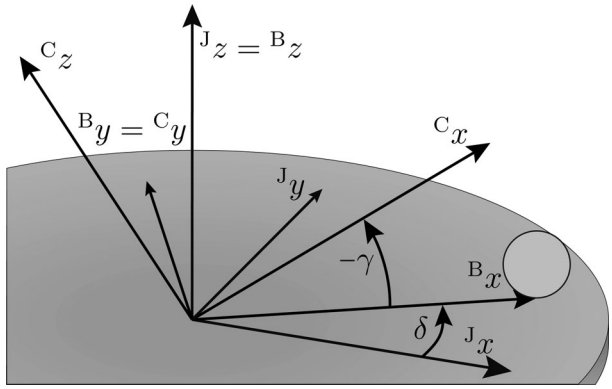

Fig. 4. Definition of coordinate systems for impact dynamics. In order to rotate the ball and paddle velocity vectors to the impact coordinate system C, we first rotate about the z-axis of the coordinate system J to the intermediate coordinate system B. The rotation angle δ is chosen such that the x-axis of B points to the impact location of the ball. Second, we rotate about the y-axis of B, such that the x-axis of C is tangential to the paddle surface at the ball impact location. Due to the right-hand rule and the concave, parabolic paddle shape, the second rotation angle is always nonpositive: $\gamma \leq 0$.

There are two rotations involved, and both are illustrated in Fig. 4. First, we rotate the coordinate system J by δ about the ${}^{\mathrm{J}}z$-axis, such that the ${}^{\mathrm{B}}x$-axis of the resulting coordinate system B points in the direction of the impact location. The corresponding rotation matrix is

$${}^{\mathrm{B}}_{\mathrm{J}}\mathrm{Q} = \begin{bmatrix} {}^{\mathrm{B}}_{\mathrm{J}}\mathrm{O} & 0 \\ 0 & {}^{\mathrm{B}}_{\mathrm{J}}\mathrm{O} \end{bmatrix}, \quad {}^{\mathrm{B}}_{\mathrm{J}}\mathrm{O} = \begin{bmatrix} \cos\delta & \sin\delta & 0 \\ -\sin\delta & \cos\delta & 0 \\ 0 & 0 & 1 \end{bmatrix} \tag{43}$$

$$\sin\delta = \frac{{}^{\mathrm{J}}y}{r}, \quad \cos\delta = \frac{{}^{\mathrm{J}}x}{r}, \quad r^2 = \left({}^{\mathrm{J}}x^2 + {}^{\mathrm{J}}y^2 \right) \tag{44}$$

given the impact location ${}^{\mathrm{J}}x$, ${}^{\mathrm{J}}y$. Note that the division by r, which is nominally zero, is not an issue since r cancels out in the first-order approximation later on. The rotation matrix ${}^{\mathrm{B}}_{\mathrm{J}}\mathrm{Q}$ transforms the ball velocity state from J to B

$${}^{\mathrm{B}}V_{\mathrm{S}} = {}^{\mathrm{B}}_{\mathrm{J}}\mathrm{Q}\, {}^{\mathrm{J}}V_{\mathrm{S}}. \tag{45}$$

The paddle velocity is not affected by this rotation, as it points in the axis of rotation

$${}^{\mathrm{B}}\dot{z}_{\mathrm{P}} = {}^{\mathrm{J}}\dot{z}_{\mathrm{P}}. \tag{46}$$

Next, we rotate the coordinate system B by γ about ${}^{\mathrm{B}}y$, such that ${}^{\mathrm{C}}x$ of the impact coordinate system is tangential to the paddle surface at the ball impact location (see Fig. 5). The rotation

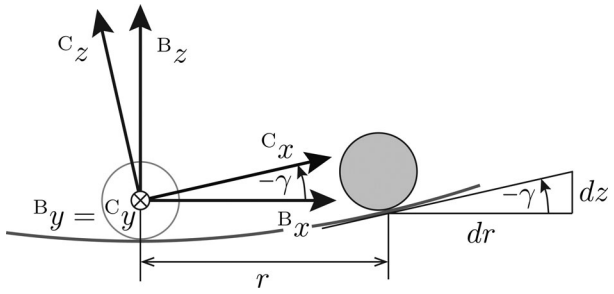

Fig. 5. Paddle surface and rotation from B to the impact coordinate system C, which is tangential to the paddle surface at the ball impact location.

matrix is

$$ {}^{\mathrm{C}}_{\mathrm{B}}\mathrm{Q} = \begin{bmatrix} {}^{\mathrm{C}}_{\mathrm{B}}\mathrm{O} & 0 \\ 0 & {}^{\mathrm{C}}_{\mathrm{B}}\mathrm{O} \end{bmatrix}, \quad {}^{\mathrm{C}}_{\mathrm{B}}\mathrm{O} = \begin{bmatrix} \cos\gamma & 0 & -\sin\gamma \\ 0 & 1 & 0 \\ \sin\gamma & 0 & \cos\gamma \end{bmatrix} \tag{47} $$

$$ \sin\gamma = -\frac{cr}{\sqrt{1+c^2r^2}}, \quad \cos\gamma = \frac{1}{\sqrt{1+c^2r^2}} \tag{48} $$

which we obtained from the derivative of the paddle shape (42) with respect to the radius (see Fig. 5)

$$ \frac{dz}{dr} = cr. \tag{49} $$

The rotation matrix ${}^{\mathrm{C}}_{\mathrm{B}}\mathrm{Q}$ transforms the ball velocity state from B to C

$$ {}^{\mathrm{C}}V_{\mathrm{S}} = {}^{\mathrm{C}}_{\mathrm{B}}\mathrm{Q}\,{}^{\mathrm{B}}V_{\mathrm{S}}. \tag{50} $$

The direct coordinate transformation from J to C is

$$ {}^{\mathrm{C}}_{\mathrm{J}}\mathrm{Q} = {}^{\mathrm{C}}_{\mathrm{B}}\mathrm{Q}\,{}^{\mathrm{B}}_{\mathrm{J}}\mathrm{Q}. \tag{51} $$

Finally, we transform the paddle velocity $\dot{z}_{\mathrm{P}}$. Since the rotation is about ${}^{\mathrm{B}}y$, the only nonzero velocities are in ${}^{\mathrm{C}}x$ and ${}^{\mathrm{C}}z$. We find

$$ \begin{bmatrix} {}^{\mathrm{C}}\dot{x}_{\mathrm{P}} \\ {}^{\mathrm{C}}\dot{z}_{\mathrm{P}} \end{bmatrix} = {}^{\mathrm{C}}_{\mathrm{J}}\mathrm{Q}_{\mathrm{P}}\,{}^{\mathrm{J}}\dot{z}_{\mathrm{P}} = \begin{bmatrix} -\sin\gamma \\ \cos\gamma \end{bmatrix} {}^{\mathrm{J}}\dot{z}_{\mathrm{P}}. \tag{52} $$

4) Horizontal Impact Model: In the derivation of the nominal trajectory, we introduced Newton's impact law for the vertical velocities (10). For the horizontal velocities and spin, we use the impact model introduced by Cross [26]. The horizontal coefficient of restitution e_x is a function of the relative ball velocity and spin, which is expressed in the impact coordinate system C as

$$ e_x := -\frac{{}^{\mathrm{C}}\dot{\hat{x}}^{+} - R\,{}^{\mathrm{C}}\omega_y^{+}}{{}^{\mathrm{C}}\dot{\hat{x}}^{-} - R\,{}^{\mathrm{C}}\omega_y^{-}} \tag{53} $$

$$ {}^{\mathrm{C}}\dot{\hat{x}} = {}^{\mathrm{C}}\dot{x} - {}^{\mathrm{C}}\dot{x}_{\mathrm{P}} \tag{54} $$

where R is the ball radius, and ${}^{\mathrm{C}}\dot{x}_{\mathrm{P}}$ the horizontal velocity of the paddle surface. The parameter e_x relates the relative horizontal velocity of the contact point of the ball over the impact. Values of e_x range from -1 to 1 and capture both gripping and slipping ball behavior. For $e_x = -1$, the impact surface is frictionless, and the relative velocity of the ball contact point does not change. For $e_x = 0$, the ball grips the surface without slipping, and "rolls" through the impact. Finally, $e_x = 1$ captures a gripping, perfectly elastic ball: The relative velocity is inverted. Positive values of e_x explain the observation that a superball ($e_x \approx 0.5$ [26]) returns to your hand when you throw it onto the floor at an angle such that it bounces off the underside of your desk.

Equation (53) does not yet fully define the postimpact ball velocity and spin. We further use conservation of angular momentum, evaluated at the ball contact point

$$ \frac{2}{5}mR^2\,{}^{\mathrm{C}}\omega_y^{+} + mR\,{}^{\mathrm{C}}\dot{x}^{+} = \frac{2}{5}mR^2\,{}^{\mathrm{C}}\omega_y^{-} + mR\,{}^{\mathrm{C}}\dot{x}^{-} \tag{55} $$

with ball mass m. We combine (53)–(55), and obtain

$$ {}^{\mathrm{C}}\dot{x}^{+} = \frac{1}{7}\left((5-2e_x)\,{}^{\mathrm{C}}\dot{x}^{-} + 2\,(1+e_x)\left({}^{\mathrm{C}}\dot{x}_{\mathrm{P}} + R\,{}^{\mathrm{C}}\omega_y^{-}\right)\right) \tag{56} $$

$$ {}^{\mathrm{C}}\omega_y^{+} = \frac{5}{7R}\left((1+e_x)\,{}^{\mathrm{C}}\dot{\hat{x}} + \left(\frac{2}{5} - e_x\right)R\,{}^{\mathrm{C}}\omega_y^{-}\right). \tag{57} $$

These equations are analogous for the states ${}^{\mathrm{C}}\dot{y}$ and ${}^{\mathrm{C}}\omega_x$. However, one must consider that, by the right-hand rule, the ball spin ${}^{\mathrm{C}}\omega_x$ has the opposite contribution to the relative velocity of the contact point and the angular momentum than ${}^{\mathrm{C}}\omega_y$. Therefore, the appropriate update equations are obtained with the substitutions ${}^{\mathrm{C}}\dot{y} = {}^{\mathrm{C}}\dot{x}$ and ${}^{\mathrm{C}}\omega_x = -{}^{\mathrm{C}}\omega_y$. We further assume $e_y = e_x$. Finally, we assume that the spin ${}^{\mathrm{C}}\omega_z$ is not affected by the impact: ${}^{\mathrm{C}}\omega_z^{+} = {}^{\mathrm{C}}\omega_z^{-}$.

5) Impact Function: We combine the horizontal [(56) and (57)] and vertical (10) impact models into a single impact function, which maps the preimpact ball and paddle velocities to the postimpact ball velocity

$$ {}^{\mathrm{C}}V_{\mathrm{S}}^{+} = {}^{\mathrm{C}}\Gamma_{\mathrm{S}}\,{}^{\mathrm{C}}V_{\mathrm{S}}^{-} + {}^{\mathrm{C}}\Gamma_{\mathrm{P}} \begin{bmatrix} {}^{\mathrm{C}}\dot{x}_{\mathrm{P}} \\ {}^{\mathrm{C}}\dot{z}_{\mathrm{P}} \end{bmatrix} \tag{58} $$

$$ {}^{\mathrm{C}}\Gamma_{\mathrm{S}} = \begin{bmatrix} 1-k & 0 & 0 & 0 & kR & 0 \\ 0 & 1-k & 0 & -kR & 0 & 0 \\ 0 & 0 & -e_z & 0 & 0 & 0 \\ 0 & -\alpha & 0 & 1-\alpha R & 0 & 0 \\ \alpha & 0 & 0 & 0 & 1-\alpha R & 0 \\ 0 & 0 & 0 & 0 & 0 & 1 \end{bmatrix} $$

$$ {}^{\mathrm{C}}\Gamma_{\mathrm{P}} = \begin{bmatrix} k & 0 \\ 0 & 0 \\ 0 & e_z+1 \\ 0 & 0 \\ -\alpha & 0 \\ 0 & 0 \end{bmatrix}, \quad \begin{aligned} \alpha &= \frac{5\,(e_x+1)}{7R} \\ k &= \frac{2\,(e_x+1)}{7}. \end{aligned} \tag{59} $$

The postimpact ball state, which is expressed in the coordinate system J, is

$$ \begin{aligned} {}^{\mathrm{J}}\widetilde{S}_2^{+} &= \mathrm{I}_{\mathrm{S}}\,{}^{\mathrm{J}}S_2^{-} \\ &\quad + \mathrm{T}_{\mathrm{VS}}^{\mathsf{T}}\,{}^{\mathrm{C}}_{\mathrm{J}}\mathrm{Q}^{\mathsf{T}}\left({}^{\mathrm{C}}\Gamma_{\mathrm{S}}\,{}^{\mathrm{C}}_{\mathrm{J}}\mathrm{Q}\,\mathrm{T}_{\mathrm{VS}}\,{}^{\mathrm{J}}S_2^{-} + {}^{\mathrm{C}}\Gamma_{\mathrm{P}}\,{}^{\mathrm{C}}_{\mathrm{J}}\mathrm{Q}_{\mathrm{P}}\mathrm{T}_{\mathrm{VP}}\,{}^{\mathrm{J}}P_2\right) \end{aligned} \tag{60} $$

where we applied the appropriate coordinate transformations. The term $\mathrm{I_S}\,{}^{\mathrm{J}}S_2^-$ accounts for the identity mapping of the ball position over the impact

$$\mathrm{I_S} = \begin{bmatrix} \mathrm{K_S} & 0 & 0 \\ 0 & \mathrm{K_S} & 0 \\ 0 & 0 & \mathrm{K_S} \end{bmatrix}, \quad \mathrm{K_S} = \begin{bmatrix} 1 & 0 & 0 \\ 0 & 0 & 0 \\ 0 & 0 & 0 \end{bmatrix}. \tag{61}$$

In the following, all states are expressed in the coordinate system J, and we omit the superscripts. Equation (60) is nonlinear because the rotation matrices ${}^{\mathrm{C}}_{\mathrm{J}}\mathrm{Q}$ (51) and ${}^{\mathrm{C}}_{\mathrm{J}}\mathrm{Q}_{\mathrm{P}}$ (52) are nonlinear functions of the preimpact ball state S_2^-. The first-order approximation of the perturbed ball state is

$$S_2^+ = \bar{S}_2^+ + \left.\frac{\partial \widetilde{S}_2^+}{\partial S_2^-}\right|_{\left(\bar{S}_2^-, \bar{P}_2\right)} s_2^- + \left.\frac{\partial \widetilde{S}_2^+}{\partial P_2}\right|_{\left(\bar{S}_2^-, \bar{P}_2\right)} p_2 \tag{62}$$

where the Jacobian matrices are evaluated at the respective nominal states. Together with the equations for the preimpact ball and paddle perturbations (38) and (39), we obtain the matrix which describes how the ball perturbations at nominal impact time s_1 map, to first order, to the postimpact ball perturbations

$$\begin{aligned} s_2^+ &= \left.\frac{\partial S_2^+}{\partial S_2^-}\right|_{\left(\bar{S}_2^-, \bar{P}_2\right)} s_2^- + \left.\frac{\partial S_2^+}{\partial P_2}\right|_{\left(\bar{S}_2^-, \bar{P}_2\right)} p_2 && (63) \\ &= \left.\frac{\partial S_2^+}{\partial S_2^-}\right|_{\left(\bar{S}_2^-, \bar{P}_2\right)} (\mathrm{I} + \dot{\bar{S}}_1 \mathrm{M}_{\tau 1}) s_1 \\ &\quad + \left.\frac{\partial S_2^+}{\partial P_2}\right|_{\left(\bar{S}_2^-, \bar{P}_2\right)} \dot{\bar{P}}_1 \mathrm{M}_{\tau 1} s_1 && (64) \\ &= \mathrm{M}_{21} s_1 && (65) \end{aligned}$$

where

$$\mathrm{M}_{21} = \begin{bmatrix} \mathrm{M}_{21}^x & 0 & 0 \\ 0 & \mathrm{M}_{21}^y & 0 \\ 0 & 0 & \mathrm{M}_{21}^z \end{bmatrix} \tag{66}$$

$$\mathrm{M}_{21}^x = \begin{bmatrix} 1 & 0 & 0 \\ \beta c(gT + \dot{\bar{z}}_{\mathrm{P}1}) & 1-k & kR \\ -\alpha c(gT + \dot{\bar{z}}_{\mathrm{P}1}) & \alpha & 1 - R\alpha \end{bmatrix} \tag{67}$$

$$\mathrm{M}_{21}^y = \begin{bmatrix} 1 & 0 & 0 \\ \beta c(gT + \dot{\bar{z}}_{\mathrm{P}1}) & 1-k & -kR \\ \alpha c(gT + \dot{\bar{z}}_{\mathrm{P}1}) & -\alpha & 1 - R\alpha \end{bmatrix} \tag{68}$$

$$\mathrm{M}_{21}^z = \begin{bmatrix} \dfrac{\dot{\bar{z}}_{\mathrm{P}1}}{gT + \dot{\bar{z}}_{\mathrm{P}1}} & 0 & 0 \\ \dfrac{a_{\mathrm{P}}\,(e_z+1) + e_z g}{gT + \dot{\bar{z}}_{\mathrm{P}1}} & -e_z & 0 \\ 0 & 0 & 1 \end{bmatrix} \tag{69}$$

$$\beta = k - 1 - e_z. \tag{70}$$

D. Second Free Fall

After impact, the ball is in free fall again. We map the perturbations s_2^+ from time $T+\tau$ to $2T+\tau$ analogous to the first free fall in Section III-B

$$s_3 = \mathrm{M}_{32} s_2^+, \quad \mathrm{M}_{32} = \mathrm{M}_{10}. \tag{71}$$

E. Final Apex

The perturbations s_3 are the ball perturbations at time $2T+\tau$. Therefore, we compensate for τ in order to obtain the ball perturbations s_4 at nominal apex time $2T$. Analogous to (32), we obtain

$$s_4 = s_3 - \dot{\bar{S}}_3 \tau = s_3 - \dot{\bar{S}}_3 \mathrm{M}_{\tau 1} s_1 \tag{72}$$

$$\dot{\bar{S}}_3 = (0,0,0,0,0,0,0,-g,0)^{\mathsf{T}} \tag{73}$$

where we used (30) and that to first order, $\dot{S}_3 \tau = \dot{\bar{S}}_3 \tau$.

F. Complete Map

We combine (22), (65), (71), and (72) to obtain the matrix M_{40}, which maps the initial perturbations s_0 to first order over a single impact

$$s_4 = \mathrm{M}_{40}\, s_0. \tag{74}$$

The matrix is

$$\mathrm{M}_{40} = \mathrm{M}_{32}\mathrm{M}_{21}\mathrm{M}_{10} - \dot{\bar{S}}_3 \mathrm{M}_{\tau 1} \mathrm{M}_{10}. \tag{75}$$

It is a block diagonal matrix with blocks corresponding to the horizontal and vertical perturbation dynamics

$$\mathrm{M}_{40} = \begin{bmatrix} \mathrm{A}_x & 0 & 0 & 0 \\ 0 & \mathrm{A}_y & 0 & 0 \\ 0 & 0 & \mathrm{A}_z & 0 \\ 0 & 0 & 0 & 1 \end{bmatrix} \tag{76}$$

$$\mathrm{A}_x = \begin{bmatrix} \frac{2c\beta gT^2}{e_z+1} + 1 & T\left(\frac{2c\beta gT^2}{e_z+1} - k + 2\right) & kRT \\ \frac{2c\beta gT}{e_z+1} & \frac{2c\beta gT^2}{e_z+1} - k + 1 & kR \\ -\frac{2cg\alpha T}{e_z+1} & \alpha - \frac{2cg\alpha T^2}{e_z+1} & 1 - R\alpha \end{bmatrix} \tag{77}$$

$$\mathrm{A}_y = \begin{bmatrix} \frac{2c\beta gT^2}{e_z+1} + 1 & T\left(\frac{2c\beta gT^2}{e_z+1} - k + 2\right) & -kRT \\ \frac{2c\beta gT}{e_z+1} & \frac{2c\beta gT^2}{e_z+1} - k + 1 & -kR \\ \frac{2cg\alpha T}{e_z+1} & -\alpha + \frac{2cg\alpha T^2}{e_z+1} & 1 - R\alpha \end{bmatrix} \tag{78}$$

$$\mathrm{A}_z = \begin{bmatrix} \frac{a_{\mathrm{P}}\,(e_z+1)^2 + g\left({e_z}^2+1\right)}{2g} & \frac{\left(g(e_z-1)^2 + (e_z+1)^2 a_{\mathrm{P}}\right)T}{2g} \\ \frac{(e_z+1)^2(g+a_{\mathrm{P}})}{2gT} & \frac{a_{\mathrm{P}}\,(e_z+1)^2 + g\left({e_z}^2+1\right)}{2g} \end{bmatrix}. \tag{79}$$

All the dependent parameters, which are summarized, are

$$T = \sqrt{\frac{2H}{g}}, \qquad k = \frac{2\,(e_x+1)}{7} \tag{80}$$

$$\alpha = \frac{5\,(e_x+1)}{7R}, \quad \beta = k - 1 - e_z. \tag{81}$$

The independent parameters, which are summarized, are, therefore, the apex height H; the vertical and horizontal coefficient of restitution e_z and e_x; the ball radius R; and the two key design parameters paddle acceleration a_{P} and curvature c.

G. Decoupling of Horizontal and Vertical Dynamics

The block diagonal structure of M_{40} shows that the dynamics of the perturbations in the state tuples $(x, \dot{x}, \omega_y)$, $(y, \dot{y}, \omega_x)$, $(z, \dot{z})$, and (ω_z) are all mutually independent, to first order.

IV. Design Parameters

With the mapping M_{40}, we analyze the local stability of the ball trajectory. The goal is to find stabilizing values for the design parameters, curvature c and paddle acceleration a_{P}, for a range of apex heights and ball properties. The mapping describes an autonomous, discrete-time, linear time-invariant system

$$s[k+1] = \mathrm{M}_{40}\, s[k] \tag{82}$$

where $s[k]$ are the perturbations at the kth nominal apex time, i.e., at $t = k2T$. The system is stable if the spectral radius ρ of M_{40} is smaller than one [27]. A spectral radius smaller than one implies that any initial perturbations $s[0]$ tend to zero as $k \to \infty$. The spectral radius of M_{40} is defined as

$$\rho\left(\mathrm{M}_{40}\right) := \max_i \left|\lambda_i\left(\mathrm{M}_{40}\right)\right| \tag{83}$$

where λ_i is the ith eigenvalue of M_{40}. Since M_{40} is block diagonal, its spectral radius is equal to the largest of the spectral radii of its diagonal blocks

$$\rho\left(\mathrm{M}_{40}\right) = \max\left\{\rho\left(\mathrm{A}_x\right), \rho\left(\mathrm{A}_y\right), \rho\left(\mathrm{A}_z\right), \rho\left(1\right)\right\}. \tag{84}$$

This is equivalent to stating that the dynamics of the perturbation tuples corresponding to the diagonal blocks must be stable. For the perturbation in vertical spin ω_z, the corresponding spectral radius is $\rho(1) = 1$, which is marginally stable. However, we ignore ω_z in the stability analysis since the dynamics in ω_z are, to first order, decoupled from all other states and have no influence on juggling. Therefore, we state that the ball trajectory is stable if $\rho\left(\mathrm{A}_x\right)$, $\rho\left(\mathrm{A}_y\right)$, and $\rho\left(\mathrm{A}_z\right)$ are smaller than one.

There are two more observations that make the stability analysis more straightforward. First, we notice that A_x and A_y are similar [28]

$$\mathrm{A}_y = \mathrm{T}_{xy}^{-1}\mathrm{A}_x\mathrm{T}_{xy}, \quad \mathrm{T}_{xy} = \begin{bmatrix} 1 & 0 & 0 \\ 0 & 1 & 0 \\ 0 & 0 & -1 \end{bmatrix} \tag{85}$$

which is based on the relation between ω_y and ω_x in the impact dynamics (see Section III-C4). The similarity implies that A_y and A_x have the same eigenvalues; ergo, they have the same spectral radius. To attain stability of all horizontal degrees of freedom of the ball, it is, therefore, sufficient to show that $\rho\left(\mathrm{A}_x\right) < 1$. Intuitively, it is expected that the horizontal ball dynamics in y are not different from the dynamics in x due to symmetry.

Second, we find that $\rho\left(\mathrm{A}_x\right)$ is independent of the paddle acceleration a_{P}, and $\rho\left(\mathrm{A}_z\right)$ is independent of the curvature c.

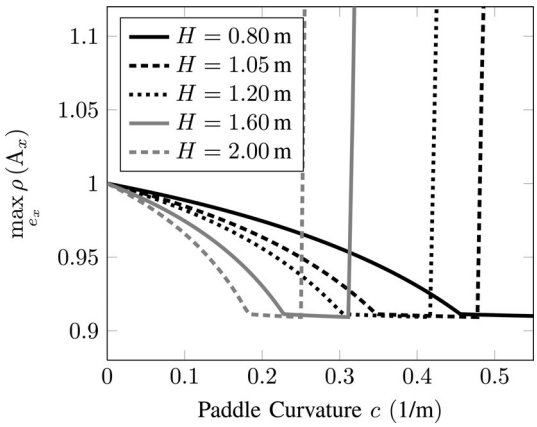

Fig. 6. Worst-case spectral radius of A_x for $e_z = 0.8$ and $e_x \in [-0.5, 0.5]$.

Therefore, we can analyze the horizontal and vertical stability of the ball trajectory separately.

MATLAB scripts featuring the following analyses are available in the multimedia files provided with this paper.

A. Horizontal Stability

Local stability of the horizontal degrees of freedom is achieved by choosing a paddle curvature that produces a spectral radius $\rho\left(\mathrm{A}_x\right)$ smaller than one. Notice how the ball radius R enters the matrix A_x (77): The only occurrences of R are in the numerator of elements (row, column) = (1,3) and (2,3) and in the denominator of elements (3,1) and (3,2), from which it is straightforward to show that the eigenvalues of A_x are independent of the ball radius.

We find that $\rho\left(\mathrm{A}_x\right)$ is sensitive to the apex height H. In contrast, the impact of the vertical coefficient of restitution e_z on the following numerical stability analysis is negligible and we fix it at $e_z = 0.8$, which lies in the middle of the interval $e_z \in [0.7, 0.9]$. This interval corresponds to the range of balls we expect to juggle: tennis balls to superballs [26]. We capture the variability of the spectral radius with respect to the unknown horizontal coefficient of restitution e_x with a worst-case analysis. In Fig. 6, we show the maximum of $\rho\left(\mathrm{A}_x\right)$ over the range $e_x \in [-0.5, 0.5]$ for various apex heights as a function of the curvature c. The parameter range chosen for e_x captures both slipping and gripping ball impact behavior as described in Section III-C4 and [26].

We set the design specification for the first robot prototype to juggle at heights of up to 1.2 m. Therefore, choosing the paddle curvature $c = 0.36$ (1/m) satisfies the stability requirement.

B. Vertical Stability

Local stability of the vertical degrees of freedom is achieved with an appropriate paddle acceleration. Inspecting A_z (79), we find that the nominal impact time T (the only parameter depending on the apex height) appears in the off-diagonal elements in such a way that it cancels out when calculating the eigenvalues of A_z. Therefore, the spectral radius $\rho\left(\mathrm{A}_z\right)$ is independent of the apex height. Analogous to the horizontal stability

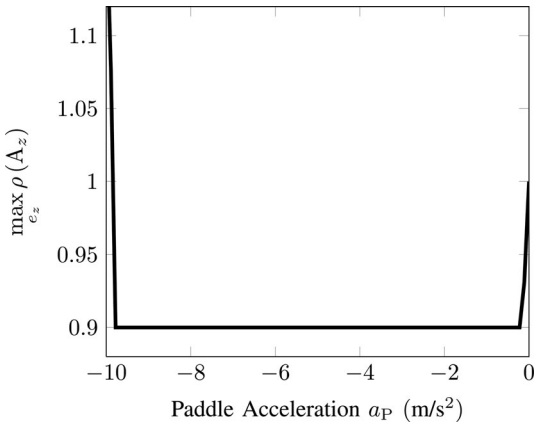

Fig. 7. Worst-case spectral radius of A_z for $e_z \in [0.7, 0.9]$.

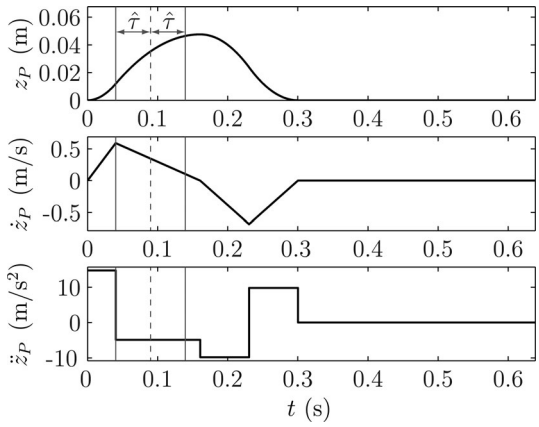

Fig. 8. Paddle trajectory for apex height $H = 0.5$ m and vertical coefficient of restitution $e_z = 0.8$. The time interval shown is equivalent to $2T$. The nominal ball impact is indicated by the dashed line, which is flanked by the deceleration intervals defined by $\hat{\tau}$. Note that the paddle position is shifted such that the lowest paddle position is at zero.

analysis, we use a worst-case analysis of $\rho(\mathrm{A}_z)$ over the range $e_z \in [0.7, 0.9]$. The resulting spectral radii are shown in Fig. 7. We choose $a_\mathrm{P} = -g/2 \approx -5$ m/s^2, which lies in the center of the stable region. The determined negative acceleration is consistent with results in the literature that show that a negative acceleration is stabilizing. See, for example, the work by Schaal and Atkeson [8] or Ronsse *et al.* [21], [22].

C. Aside: Alternative States for Perturbation Mapping

Perturbation maps, i.e., Poincaré maps, are often defined between impact events in the impact juggling literature, e.g., in [19]. In contrast, we choose a fixed time interval for the mapping M_{40} between the ball apex states. This choice is motivated by the analysis of a periodic ball motion driven by an open-loop paddle motion with a fixed period time. One can show, however, that the two representations are equivalent, to first order. We define the alternative ball state as $\hat{S} := (x, \dot{x}, \omega_y, y, \dot{y}, \omega_x, t, \dot{z}, \omega_z)$, with t the impact time, and the other states defined as the positions, velocities, and spins just before impact. We may then analyze the local stability of the nominal ball trajectory with the linearized Poincaré map for the alternative perturbations $\hat{s}$, where the perturbation in impact time is τ (29). One can show that to first order

$$\hat{s} = \mathrm{T}_{\hat{s}s} s \tag{86}$$

where

$$\mathrm{T}_{\hat{s}s} = \begin{bmatrix} \mathrm{T}^{xy}_{\hat{s}s} & 0 & 0 & 0 \\ 0 & \mathrm{T}^{xy}_{\hat{s}s} & 0 & 0 \\ 0 & 0 & \mathrm{T}^{z}_{\hat{s}s} & 0 \\ 0 & 0 & 0 & 1 \end{bmatrix}, \quad \mathrm{T}^{xy}_{\hat{s}s} = \begin{bmatrix} 1 & T & 0 \\ 0 & 1 & 0 \\ 0 & 0 & 1 \end{bmatrix} \tag{87}$$

$$\mathrm{T}^{z}_{\hat{s}s} = \frac{1}{gT + \dot{\hat{z}}_{\mathrm{P}1}} \begin{bmatrix} 1 & T \\ -g & \dot{\hat{z}}_{\mathrm{P}1} \end{bmatrix}. \tag{88}$$

Therefore

$$\hat{s}[k+1] = \mathrm{T}_{\hat{s}s} s[k+1] = \mathrm{T}_{\hat{s}s} \mathrm{M}_{40} s[k] = \mathrm{T}_{\hat{s}s} \mathrm{M}_{40} \mathrm{T}^{-1}_{\hat{s}s} \hat{s}[k]. \tag{89}$$

The inverse $\mathrm{T}^{-1}_{\hat{s}s}$ is well defined for $T > 0$. It follows that the mapping matrices for $\hat{s}$ and s are similar [28], and therefore, the maps have the same eigenvalues. Furthermore, the block diagonal structure of $\mathrm{T}_{\hat{s}s}$ preserves the decoupling of the marginally stable ω_z from the other states in $\hat{s}$. Therefore, the stability of the remaining states directly follows from the stability of A_x, A_y, and A_z. Intuitively, if the perturbations at the ball apex vanish as the number of impacts tends to infinity, the ball impact time deviations τ vanish as well.

V. Blind Juggler

We built a first prototype of the Blind Juggler with the determined paddle curvature $c = 0.36$ (1/m) and paddle acceleration $a_\mathrm{P} = -g/2$. An industrial linear motor (Linmot PS01-37×120 [29]) actuates the solid aluminum paddle, which was CNC-milled to the desired shape and has a diameter of 0.3 m. We sized the motor to be able to continuously juggle balls with a coefficient of restitution e_z of at least 0.7 (tennis ball) and at apex heights H up to at least 1.2 m.

The trajectory of the paddle is tracked by a servo controller (B1100, also by Linmot [29]). We manually tuned the servo controller to produce acceptable tracking performance. A high-level state machine running on a D-Space real-time control system [30] provides the profile parameters to the servo controller and times the motion.

A. Paddle Trajectory

For a given coefficient of restitution e_z and apex height H, the paddle state at nominal impact is defined by (9) and (11). Before and after the nominal ball impact, the paddle decelerates with a_P for time $\hat{\tau}$ (see Fig. 8). Initially, we determined $\hat{\tau}$ by assuming a static error in the ball coefficient of restitution. As we obtained measurements of the impact times, however, we fixed $\hat{\tau}$ based on impact time deviation statistics. We found that $\hat{\tau} = 0.05$ s works well.

In practice, a larger $\hat{\tau}$ increases vertical robustness since larger impact time deviations are still within the stabilizing deceleration interval of the paddle trajectory. In addition, a larger $\hat{\tau}$ enables the robot to juggle balls with a wider range of coefficients of restitution. A ball with a coefficient of restitution different from the one the trajectory is designed for results in a shift in mean impact time. For example, a ball with a lower coefficient of restitution results in an earlier mean impact time where the paddle is faster. Therefore, it is desirable to achieve a larger range of paddle velocities during the deceleration interval. A larger range is also achieved by a higher paddle deceleration a_{P}, given a fixed $\hat{\tau}$. In fact, it can be shown that for a given velocity range, a higher deceleration is preferable over a larger $\hat{\tau}$, since it leads to a smaller total stroke of the paddle. There is a tradeoff, however, since a higher paddle deceleration leads to wider impact time distributions (see Section VI-C), which in turn requires a longer deceleration time $\hat{\tau}$.

Finally, we choose the accelerations to speed up the paddle before decelerating during impact, and for retracting. We use an acceleration of 15 m/s^2 to speed up the paddle and accelerations of ± 10 m/s^2 for the retracting motion. A sample paddle trajectory is shown in Fig. 8.

B. First Results

The first prototype of the Blind Juggler is able to continuously juggle a variety of balls at heights between a few centimeters and about 1.4 m. Heights above 0.6 m are only achieved with small Nylon precision balls; see the ball discussion in Section V-C. The Blind Juggler is robust to both horizontal and vertical perturbations.

1) Vertical: The apex height may be changed by slowly adapting the paddle motion. A given nominal apex height defines the paddle motion, as discussed in Section V-A. If the nominal apex height, and, therefore, the paddle trajectory, is changed between two impacts of the ball by a small amount, the ball transitions to the new apex height due to the vertical local stability. This is demonstrated in a video provided with this paper. In the video, the nominal apex height is increased by 0.08 m between impacts until the ball reaches the desired height.

2) Horizontal: We tested horizontal robustness by slowly pushing the robot back and forth in a wheeled cart. This demonstration is documented in a video provided with this paper.

C. Impact of Ball Properties on Performance

In experiments with different balls, we observe that the main source of noise in the measured impact times and locations are stochastic deviations of the impact parameters, i.e., ball roundness and coefficient of restitution. Solid Nylon balls, which are manufactured to precise roundness for valve applications, introduce the least amount of noise. Specifically, we use precision balls that have a diameter of 0.012 m and that weigh 0.001 kg. Only these precision balls allow the robot to juggle at apex heights larger than 0.6 m. Inferior balls, such as superballs and table tennis balls, bounce too far off-center and eventually fall off the paddle at larger apex heights. High-quality table tennis balls provide reasonable roundness tolerances but still fall off at larger heights. We suspect that the seam where the half-spheres are joined causes the balls to bounce off-center. Others suggested that for larger balls, aerodynamic effects may introduce additional horizontal ball motion. The behavior of different balls on the robot is demonstrated in a video provided with this paper.

D. Measurements

We measured the impact time of the ball using a microphone. The impact locations on the paddle were measured using a video camera mounted above the paddle. Whenever the microphone detects an impact, a small LED array lights up that is visible to the video camera. In an offline image analysis step, we extracted the relative positions of the ball to the paddle from all video frames where the LED array is lit. In addition, we measured the paddle position and velocity at impact with the motor encoder.

Given the measurement data, we estimated parts of the ball state trajectory between two impacts. Since we had no measurements of the ball spin available, we only estimated the states $x, \dot{x}, y, \dot{y}, z$, and $\dot{z}$. We did not consider aerodynamic effects such as drag. Therefore, given two impact times $t[i]$ and $t[i-1]$, and the corresponding impact locations $x[i]$ and $x[i-1]$, the constant ball velocity between the impacts is $\dot{x}[i] = (x[i] - x[i-1])/(t[i] - t[i-1])$ (y is analogous). Similarly, we estimated incoming and outgoing vertical ball velocities $\dot{z}^+[i], \dot{z}^-[i]$ given the paddle positions and the impact time difference. From the same data, we further estimated the ball height at nominal apex time.

In the following, we present experimental apex height and impact location data. All apex height data presented in this paper were obtained with the same ball and paddle in order to obtain comparable results. All measurements were performed with the high precision balls discussed in Section V-C. We collected data at three different nominal apex heights: 0.5, 0.8, and 1.05 m. All data, MATLAB scripts for its analysis, and a measurement video are available in the multimedia files provided with this paper.

1) Apex Height: The estimated height deviation of the ball at nominal apex time is equivalent to the vertical position perturbation s_{z0} (14). Means and standard deviations σ_z from experiments at different apex heights are summarized in Table I. Due to the high number of samples, we obtained submillimeter 95% confidence intervals for all means and variances shown in the table. The small nonzero means are due to modeling errors, such as imperfect trajectory tracking of the paddle, or differences between the assumed and actual ball vertical coefficient of restitution e_z. In Fig. 9, we show a histogram of the deviations at apex height $H = 1.05$ m.

2) Impact Locations: The measured impact x-location means and standard deviations σ_x are summarized in Table I. The small nonzero means are due to slightly misleveled paddles. We do not state the statistics for the impact locations in y-direction, as they are practically identical (the data are available in the multimedia files). In Fig. 10, we show a histogram of the measured impact x-locations for $H = 1.05$ m. A frame of the measurement video for the same apex height with an

TABLE I
VERTICAL AND HORIZONTAL EXPERIMENTAL DATA

Apex Height Deviation Statistics, $a_{\mathrm{P}} = -g/2$			
Height (m)	σ_z (mm)	Mean (mm)	Number of Samples
0.5	2.0	3.2	1074
0.8	3.4	3.0	1180
1.05	5.5	1.0	1079
Impact x-Location Statistics, $c = 0.36$ (1/m)			
Height (m)	σ_x (mm)	Mean (mm)	Number of Samples
0.5	12.0	3.3	5301
0.8	13.4	5.9	4549
1.05	16.3	3.3	5789

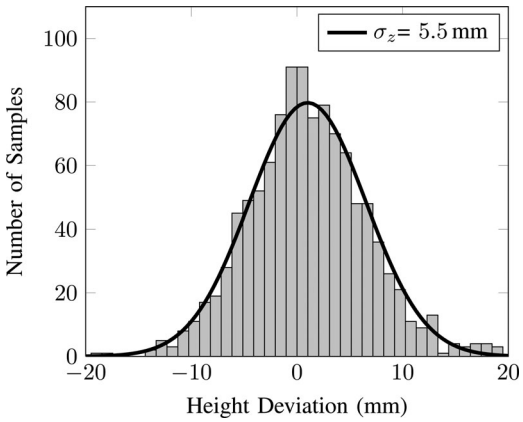

Fig. 9. Apex height deviation histogram and fitted Gaussian distribution for apex height $H = 1.05$ m.

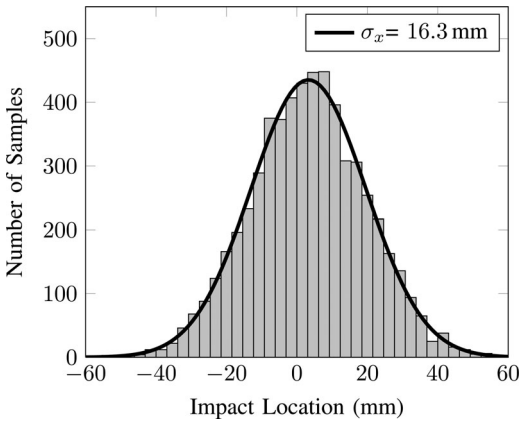

Fig. 10. Impact x-coordinate histogram and fitted Gaussian distribution for apex height $H = 1.05$ m.

overlay of all measured impact locations is shown in Fig. 11, which illustrates the narrow impact location distribution.

E. Ball Parameter Identification

1) Vertical: We identify the vertical coefficient of restitution e_z from the measured data using least squares fits. We minimize

$$\sum_{i=0}^{N-1} \left(\nu_z[i](e_z)\right)^2 \tag{90}$$

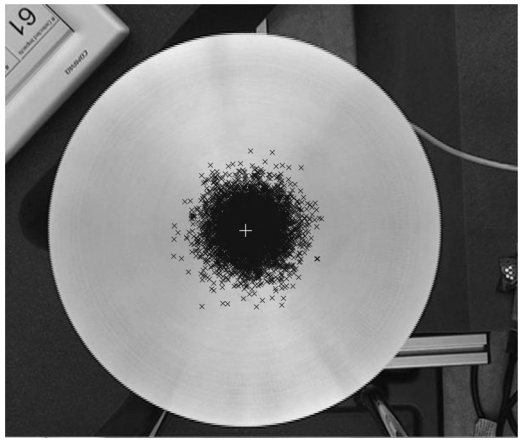

Fig. 11. Accumulated impact locations on the paddle for apex height $H = 1.05$ m. The black crosses mark the impact locations and the white cross marks the paddle center. As a reference for scale, the paddle diameter is 0.3 m.

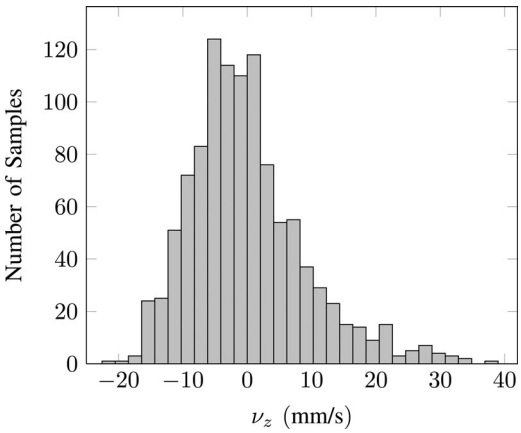

Fig. 12. Vertical process noise histogram for apex height $H = 1.05$ m. Apparently, the distribution is not Gaussian. The estimated standard deviation is $\sigma_{\nu z} = 9.09$ mm/s.

over e_z, where N is the number of measurements, and

$$\nu_z[i](e_z) := \dot{z}^+[i] + e_z \dot{z}^-[i] - (1 + e_z)\dot{z}_P[i] \tag{91}$$

is the deviation of the measured vertical postimpact ball velocity from the value that is predicted by Newton's impact model (10). From the measurements, we have $\dot{z}^+[i]$, $\dot{z}^-[i]$, and $\dot{z}_P[i]$ available (see Section V-D). The identified e_z are 0.82, 0.81, and 0.80 for the apex heights $H = 0.5,\ 0.8,\ 1.05$ m, respectively.

The signal $\nu_z[i]$ may be interpreted as process noise that is introduced into the system. The sources of this noise may include imperfect velocity tracking of the paddle, anisotropic and stochastic ball impact properties, and other modeling errors. We show a histogram of $\nu_z[i]$ for the apex height $H = 1.05$ m in Fig. 12. The data for the other heights are available in the multimedia files. The measured signals for all heights have a mean smaller than 0.01 mm/s, i.e., practically zero.

2) Horizontal: Without measuring the spin of the ball, we cannot estimate the horizontal coefficient of restitution e_x from (53). Therefore, we use a modified horizontal impact model that

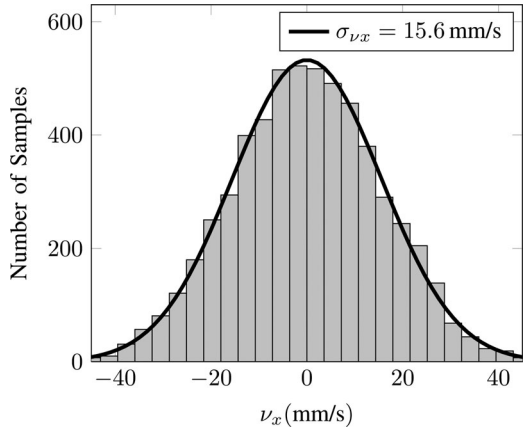

Fig. 13. Horizontal process noise histogram and fitted Gaussian distribution for apex height $H = 1.05$ m.

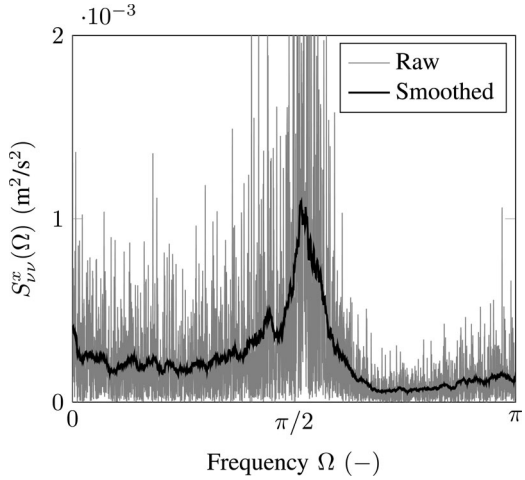

Fig. 14. PSD of horizontal process noise ν_x for apex height $H = 1.05$ m.

does not include the ball spin

$$ {}^{\mathrm{C}}\dot{x}^{+} = \epsilon\, {}^{\mathrm{C}}\dot{x}^{-} + (1-\epsilon)\, {}^{\mathrm{C}}\dot{x}_P \tag{92} $$

where ϵ is a modified horizontal coefficient of restitution, $\dot{x}_P$ is the horizontal paddle velocity, and the superscript C denotes that the states are expressed in the impact coordinate system (see Fig. 4). Similar to the vertical e_z (10), ϵ models dissipation due to friction during the impact. It can be obtained from the definition of e_x (53) by $\epsilon = -e_x \left({}^{\mathrm{C}}\omega^{-} = {}^{\mathrm{C}}\omega^{+} = 0\right)$. Since a reversal of the horizontal velocity is only plausible with ball spin present (56), ϵ may only assume values in the range of $[0, 1]$.

We identify the modified horizontal coefficient of restitution ϵ using a linearized impact model, which is analogous to (62) in the perturbation analysis. The linearized impact model for the horizontal ball velocity is

$$ \dot{x}^{+} = -c\,(\epsilon + e_z)\,(\dot{\tilde{z}}_{\mathrm{P1}} - \dot{\tilde{z}}_1)\,x + \epsilon\dot{x}^{-} + (1-\epsilon)\,\dot{x}_P \tag{93} $$

where all the states are expressed in the coordinate system J. Nominally, the horizontal paddle velocity $\dot{x}_P$ is zero; in practice, however, it is nonzero due to a misleveled paddle. We combine the term $(1-\epsilon)\,\dot{x}_P$ into a single parameter ζ, which we identify as well. We minimize

$$ \sum_{i=0}^{N-1} \left(\nu_x[i](\epsilon,\zeta)\right)^2 \tag{94} $$

over ϵ and ζ, where

$$ \nu_x[i](\epsilon,\zeta) := \dot{x}^{+}[i] + c\,(\epsilon+e_z)\,(\dot{\tilde{z}}_{\mathrm{P1}} - \dot{\tilde{z}}_1)\,x[i] - \epsilon\dot{x}^{-}[i] - \zeta. \tag{95} $$

The measurements provide the ball speeds $\dot{x}^{+}[i]$ and $\dot{x}^{-}[i]$, as well as the impact location $x[i]$. The vertical coefficient of restitution e_z is identified in a preceding step (see Section V-E1) using the vertical data from the same experiment. The nominal values $\dot{\tilde{z}}_1$ and $\dot{\tilde{z}}_{\mathrm{P1}}$ are calculated using (6) and (11). Finally, we find $\epsilon = 0.70$, 0.55, and 0.41, and $\zeta = 6.3$, 12.7, and 7.2 mm/s for apex heights $H = 0.5, 0.8,$ and 1.05 m, respectively.

We show a histogram of the noise signal $\nu_x[i]$ for the apex height $H = 1.05$ m in Fig. 13. The signal is zero mean due to the parameter ζ. We do not state the statistics for the noise introduced in the y-direction, as they are practically identical. Measurement data in y, and at other apex heights, are available in the multimedia files provided with this paper.

F. Process Noise Characteristics

We further analyzed the PSD functions of the measured noise signals ν_x and ν_z. We use the PSDs in the parameter optimization presented later on. The PSD function of the signal $\nu_x[i]$ with length N is the discrete Fourier transform of its autocorrelation function

$$ S^x_{\nu\nu}(\Omega_k) = \sum_{n=0}^{N-1} R^x_{\nu\nu}[n] e^{-j\Omega_k n} \tag{96} $$

where

$$ \Omega_k = \frac{2\pi k}{N}, \quad k = \{0, 1, \ldots, N-1\} \tag{97} $$

are the discrete frequencies, and

$$ R^x_{\nu\nu}[n] = \frac{1}{N} \sum_{i=0}^{N-1} \nu_x[i]\nu_x[i-n] \tag{98} $$

is the autocorrelation function. We calculate the autocorrelation function with wrap-around, i.e., we assume that the noise signal is periodic: $\nu_x[i + lN] = \nu_x[i]$, for any integer l. We show the measured PSD for the apex height $H = 1.05$ m in Fig. 14 for the horizontal data and in Fig. 15 for the vertical data. In the horizontal PSD, there is a significant amount of power present around the frequency $\Omega = \pi/2$. This is most likely due to the spin dynamics that are not captured in the modified horizontal impact model. Evident from both vertical and horizontal PSDs is that the noise signals are not white, since the PSDs are not flat.

VI. Design Parameter Optimization

For the first prototype of the Blind Juggler, we had to choose from a range of stabilizing design parameters. For example, the model predicts that any curvature $c \in (0, 0.42]$ keeps the ball

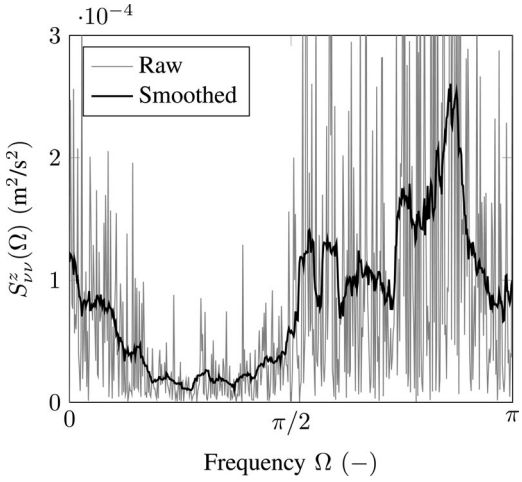

Fig. 15. PSD of vertical process noise ν_z for apex height $H = 1.05$ m.

from falling off the paddle for an apex height of $H = 1.2$ m. But how do we choose the specific value? Intuitively, one would not choose a value that is close to the boundary of the stable parameter interval shown in Fig. 6 for reasons of "robustness." Another idea would be to choose a curvature that results in the smallest spectral radius as, roughly speaking, the spectral radius is a measure for the decay rate of the system states. In the following, we use a simple scalar dynamical system to show that both of these intuitions may be misleading, and that the spectral radius may not be a good performance metric for a system. Consider the system

$$\begin{aligned} x[k+1] &= ax[k] + \frac{1}{a}\nu[k] \\ w[k] &= x[k] \end{aligned} \tag{99}$$

with state x, noise input ν, output w, and free system parameter a. We call this system $G(a)$. The goal is to keep the system output w small in the presence of some process noise ν. The spectral radius is equal to $|a|$, and therefore, we may choose any $|a| < 1$ in order to obtain a stable system.

Considering only the two intuitive criteria stated earlier, we would choose $a = 0$, which results in the smallest possible spectral radius and is also furthest from the boundary of the stable parameter region. However, the process noise enters the system through the input gain $1/a$, which gets very large for small a. Therefore, even though the state decays very quickly for small a, the noise is greatly amplified and will produce large outputs w. A good value for a must, therefore, be a tradeoff between input gain and state decay rate.

We analyze this tradeoff for the system (99) with the H_2-norm for discrete-time, linear time-invariant (LTI) systems [31]. Roughly speaking, the H_2 system norm is the gain of a system if the input is white noise. For example, the H_2 norm of the aforementioned system is the standard deviation of the output w if the noise input ν is unit variance, zero-mean white noise. The norm, which is denoted by subscript H2, is

$$\|G(a)\|^2_{\mathrm{H2}} := \frac{\mathrm{E}(w^2)}{\mathrm{E}(\nu^2)} \tag{100}$$

where E is the expected value. The norm can be calculated using the impulse response $h[k]$ of the system

$$\left\|G(a)\right\|^2_{\mathrm{H2}} = \sum_{k=-\infty}^{\infty} h^2[k] = \sum_{k=1}^{\infty}\left(\frac{1}{a}a^{k-1}\right)^2 \tag{101}$$

$$= \frac{1}{a^2}\sum_{k=0}^{\infty} a^{2k} = \frac{1}{a^2\left(1-a^2\right)}. \tag{102}$$

The tradeoff discussed previously is reflected in the structure of the denominator of the norm. The $(1 - a^2)$ factor reflects the influence of the spectral radius. In order to achieve a low norm, i.e., low output variance, the factor suggests a small a. However, there is also the contribution a^2 of the input gain factor, suggesting a large a. The minimizing a is straightforward to find. It is $a^* = \sqrt{2}/2 \approx 0.7$. If the process noise ν was indeed white, it would be optimally rejected by choosing $a = a^*$.

A. Output Variance From Input Power Spectral Density

In order to optimize juggling performance by rejecting the process noise, we use an approach analogous to the H_2 analysis in the previous section. We learned from the measurements that the process noise cannot be well approximated by white noise (see Section V-F). Therefore, we use the measured noise PSDs together with an LTI model of the juggling system in order to predict the output variances. Finally, we optimize the system parameters with the objective of minimizing the predicted output variances. For example, we analyze the horizontal system, which describes how the process noise ν_x maps to the impact location on the paddle. We then find the paddle curvature that minimizes the predicted variance of the impact locations.

The variance of the measured noise signal sequence $\nu_x[k]$ of length N may be estimated by

$$\sigma^2_{\nu x} = \frac{1}{N}\sum_{k=0}^{N-1}\nu_x^2[k] \tag{103}$$

since the signal has zero mean. This corresponds to the zero-lag value of the autocorrelation function, $R^x_{\nu\nu}[0]$ (98). Therefore, we obtain an estimate of the variance from the inverse Fourier transform of the PSD

$$\sigma^2_{\nu x} = R^x_{\nu\nu}[0] = \frac{1}{N}\sum_{k=0}^{N-1} S^x_{\nu\nu}\left(\Omega_k\right) e^{j\Omega_k \cdot 0}. \tag{104}$$

The PSD of the output w_x of a single-input, single-output, discrete-time LTI system G_x may be calculated given the PSD $S^x_{\nu\nu}$ of the noise input

$$S^x_{ww}(\Omega_k) = \left|G_x\left(\Omega_k\right)\right|^2 S^x_{\nu\nu}\left(\Omega_k\right) \tag{105}$$

where $|G_x(\Omega_k)|$ denotes the magnitude of the frequency response of the system G_x. Using the relation in (104), we may then estimate the variance of the output (because the system is linear and the input is zero-mean, the output is also zero-mean).

Analogous to the stability analysis in Section IV, we optimize the design parameters paddle curvature c and acceleration a_{P} independently for the horizontal and vertical degrees of freedom as the respective systems are decoupled to first order. MATLAB

scripts performing the following optimizations are available in the multimedia files provided with this paper.

B. Optimized Paddle Curvature

We find the paddle curvature c that minimizes the variance of the impact locations. First, we derive the input–output representation of the system for the horizontal directions based on the modified impact model (92) that is governed by the modified horizontal coefficient of restitution ϵ. We define the discrete-time LTI system G_x

$$\begin{aligned} X[k+1] &= \mathrm{A}_x^{\epsilon} X[k] + \mathrm{B}_x \nu_x[k] \\ w_x[k] &= \mathrm{C}_x X[k]. \end{aligned} \tag{106}$$

The state is $X = (s_{x0}, s_{\dot{x}0})^{\mathsf{T}}$, the horizontal perturbations at nominal apex time. The system output w_x is equivalent to the impact location on the paddle, to first order, which is what we want to keep small. The input ν_x is the horizontal process noise. The underlying sampling time is $2T$, the time between two apexes. The matrices are straightforward to derive from a perturbation analysis analogous to that in Section III and are

$$\begin{aligned} \mathrm{A}_x^{\epsilon} &= \begin{bmatrix} 1 - \frac{2c(\epsilon+e_z)gT^2}{e_z+1} & T\left(-\frac{2c(\epsilon+e_z)gT^2}{e_z+1} + \epsilon + 1\right) \\ -\frac{2c(\epsilon+e_z)gT}{e_z+1} & \epsilon - \frac{2c(\epsilon+e_z)gT^2}{e_z+1} \end{bmatrix} \\ \mathrm{B}_x &= \begin{bmatrix} T \\ 1 \end{bmatrix}, \qquad \mathrm{C}_x = \begin{bmatrix} 1 & T \end{bmatrix}. \end{aligned} \tag{107}$$

We use the system G_x and the relations (104), and (105) to predict the impact location variance as a function of the paddle curvature c. We calculate

$$\begin{aligned} \sigma_x^2(c) &= \frac{1}{N}\sum_{k=0}^{N-1} S_{ww}^x(\Omega_k, c) \\ &= \frac{1}{N}\sum_{k=0}^{N-1} \left|G_x(\Omega_k, c)\right|^2 S_{\nu\nu}^x(\Omega_k). \end{aligned} \tag{108}$$

We show the magnitude of the frequency response of the system, along with the smoothed measured PSD of the noise input signal in Fig. 16. We use the standard deviation of the output as the objective function to find the optimal noise-rejecting curvature from

$$\min_c \sigma_x(c) \tag{109}$$

for apex height $H = 1.05$ m and previously identified vertical coefficient of restitution $e_z = 0.79$ and modified horizontal coefficient of restitution $\epsilon = 0.41$. A plot of the standard deviation $\sigma_x(c)$ is shown in Fig. 17. There are two local minima at curvatures of 0.18 (1/m) and 0.39 (1/m). The minima are not very pronounced; in the interval $c = [0.18, 0.39]$, the standard deviation is constant and equal to 18 mm when rounded to millimeters. Therefore, we predict similar impact location statistics for all curvatures in this interval.

These results further illustrate the poor correlation between the spectral radius and the system performance. For $H = 1.05$ m, we find that the spectral radius of A_x is lowest for $c \in [0.35, 0.48]$ (see Fig. 6). However, Fig. 17 shows that for curvatures above 0.4 (1/m), there is a steep increase in predicted impact location standard deviation.

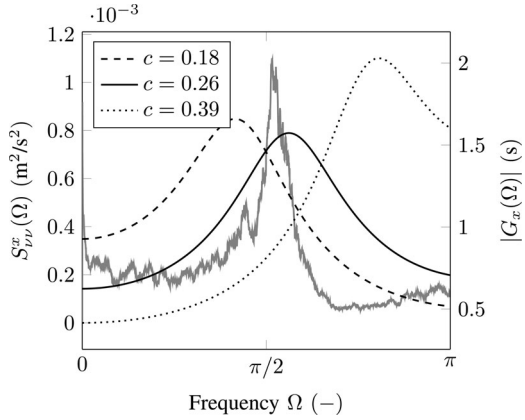

Fig. 16. Horizontal process noise smoothed PSD function from Fig. 14 (gray) and magnitude of frequency responses of the system G_x for different values of the paddle curvature.

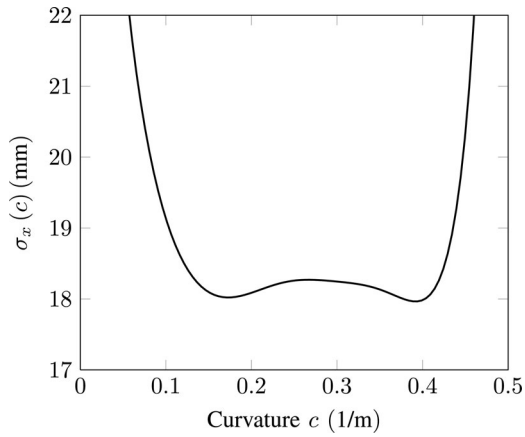

Fig. 17. Objective function of horizontal parameter optimization.

Given that the impact location standard deviations are roughly identical for all curvatures in $c = [0.18, 0.39]$, we may choose a curvature based on other criteria. Namely, we observe that the worst-case spectral radius analysis in Fig. 6 shows that lower paddle curvatures allow juggling at higher apex heights. There is a tradeoff between lower curvatures and required leveling accuracy, however. The flatter the curvature, the larger the shifts in mean impact location when the paddle is misleveled. A first-order approximation to the lower bound Δx of the expected shift in impact location is $\Delta x = \Delta\vartheta/c$, where $\Delta\vartheta$ (rad) is the leveling error angle. This bound does not include the additional shift caused by the nonzero horizontal paddle velocities due to $\Delta\vartheta$. For a curvature of $c = 0.18$ (1/m), a 1° offset would cause the ball to shift at least 0.1 m.

With the aforementioned tradeoff in mind, we manufactured a paddle with a curvature of $c = 0.24$ (1/m), for which the stability analysis predicts stable juggling at heights of up to 2 m. We achieved sustained juggling at this height in experiments and show this in a video provided with this paper.

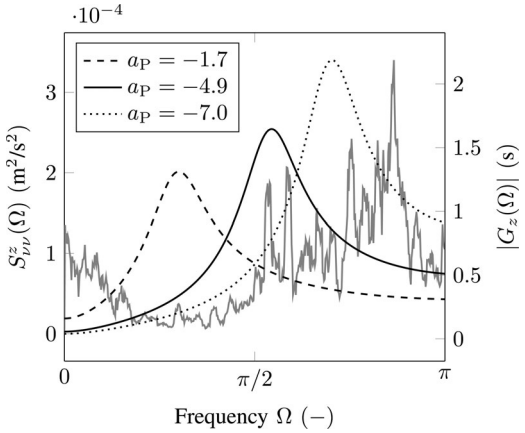

Fig. 18. Vertical process noise smoothed PSD function from Fig. 15 (gray) and magnitude of frequency responses of the system G_z for different values of the paddle acceleration.

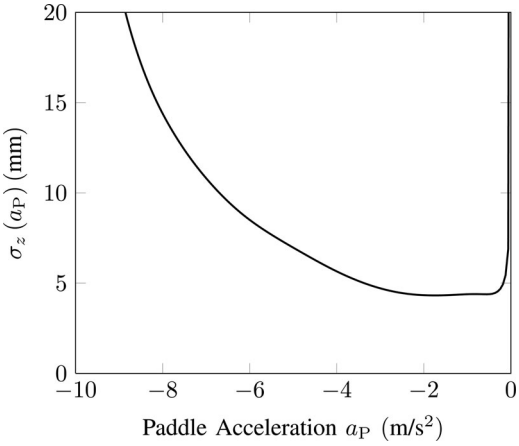

Fig. 19. Objective function of vertical parameter optimization.

C. Optimized Paddle Acceleration

Analogous to the paddle shape optimization, we optimize the paddle acceleration a_{P} to minimize the standard deviation of the apex height. We define the discrete-time LTI system G_z

$$\begin{aligned} Z[k+1] &= \mathrm{A}_z Z[k] + \mathrm{B}_z \nu_z[k] \\ w_z[k] &= \mathrm{C}_z Z[k]. \end{aligned} \tag{110}$$

The state is $Z = (s_{z0}, s_{\dot{z}0})^{\mathsf{T}}$, the vertical perturbations at nominal apex time. The output corresponds to the apex height deviation, to first order, which is equivalent to s_{z0}. The underlying sampling time is $2T$. We reuse A_z (79) from the perturbation analysis. The other system matrices are

$$\mathrm{B}_z = \begin{bmatrix} T \\ 1 \end{bmatrix}, \qquad \mathrm{C}_z = [1, 0]\,. \tag{111}$$

We predict the output variance analogously to before (108)

$$\begin{aligned} \sigma_z^2\,(a_{\mathrm{P}}) &= \frac{1}{N} \sum_{k=0}^{N-1} S^z_{ww}(\Omega_k, a_{\mathrm{P}}) \\ &= \frac{1}{N} \sum_{k=0}^{N-1} \left|G_z\,(\Omega_k, a_{\mathrm{P}})\right|^2 S^z_{\nu\nu}(\Omega_k). \end{aligned} \tag{112}$$

We show the magnitude of the frequency response of the system, along with the smoothed measured PSD of the noise input signal in Fig. 18. We obtain $a_{\mathrm{P}} = -1.75$ m/s^2 from

$$\min_{a_{\mathrm{P}}} \sigma_z\,(a_{\mathrm{P}}) \tag{113}$$

for apex height $H = 1.05$, and previously identified vertical coefficient of restitution $e_z = 0.80$. A plot of the standard deviation $\sigma_z\,(a_{\mathrm{P}})$ is shown in Fig. 19. The minimized standard deviation is $\sigma_z = 4.3$ mm. The standard deviation for $a_{\mathrm{P}} = -g/2 \approx -4.9$ m/s^2 is 6.8 mm; thus, the predicted improvement is 37% using the optimized acceleration.

In an experiment, we gathered impact data for $a_{\mathrm{P}} = -1.75$ m/s^2 using the same ball and paddle as for the measurements at $a_{\mathrm{P}} = -g/2$ presented in Table I. The measured apex height standard deviation is $\sigma_z = 4.0$ mm with 95% confidence interval of [3.88, 4.22]. Given the measured standard deviation for $a_{\mathrm{P}} = -g/2$ of $\sigma_z = 5.5$ mm, the improvement is 27%.

The process noise PSD measured at $a_{\mathrm{P}} = -1.75$ m/s^2 is, not surprisingly, different from the spectrum measured at $a_{\mathrm{P}} = -g/2$. A contributing factor is that the paddle velocity tracking errors depend on the desired paddle acceleration a_{P}. In addition, different precision balls produce different noise spectra. With the new measured noise power spectrum, we could repeat the optimization, find the optimal acceleration, and obtain new measurements. This could be extended into an iterative scheme with no guarantees of convergence to an optimal paddle acceleration. Since the measured spectra depend on a range of system parameters, and since the optimized vertical juggling performance is acceptable, we did not pursue this strategy further.

Finally, even though the measured improvement of 27% is large, it is hardly noticeable when watching the Blind Juggler bounce a ball. A higher deceleration is, in fact, often preferable, as it allows the robot to juggle balls with a larger range of coefficients of restitution; see the discussion in Section V-A. A video demonstrating the high vertical juggling performance with a closeup of ball apexes, for both $a_{\mathrm{P}} = -g/2$ and $a_{\mathrm{P}} = -1.75$ m/s^2, is available in the multimedia files provided with this paper.

VII. Conclusion

The Blind Juggler has demonstrated that high-performance robotic juggling of unconstrained balls is possible without feedback. We have analytically showed local stability of the ball trajectory and verified the results in experiments that confirmed the robot's ability to continuously juggle balls at heights of up to 2 m. We would like to highlight how signal processing concepts, such as predicting system performance from measured noise PSDs, may be used to optimize hardware design. The procedure of building a first prototype, obtaining noise measurements, and subsequent design optimization may be useful for other mechanical robot designs.

The results obtained with the Blind Juggler allow us to design more advanced juggling robots, for example, the Pendulum

Juggler, which is able to juggle unconstrained balls in a side-to-side pattern without feedback [32]. We further developed a paddle that features four concave, parabolic areas which enabled the Blind Juggler to simultaneously juggle up to four balls. We used this paddle to study the rich dynamics of the bouncing ball system, such as coexisting stable periodic orbits and chaotic system behavior. Additional information, including videos, may be found on the project website: www.blindjuggler.org.

ACKNOWLEDGMENT

The authors would like to thank M. Donovan and D. Burch for their great help with the mechanical and electrical design of the Blind Juggler. They would further like to thank M. Fässler for his help with the measurement setup. Finally, they are also indebted to the anonymous reviewers and S. Trimpe for their valuable suggestions and comments.

REFERENCES

[1] P. Reist and R. D'Andrea, "Bouncing an unconstrained ball in three dimensions with a blind juggling robot," in *Proc. IEEE Int. Conf. Robot. Autom.*, 2009, pp. 1774–1781.
[2] P. J. Holmes, "The dynamics of repeated impacts with a sinusoidally vibrating table," *J. Sound Vibrat.*, vol. 84, pp. 173–189, Sep. 1982.
[3] N. B. Tufillaro, T. Abbot, and J. Reilly, *An Experimental Approach to Nonlinear Dynamics and Chaos*. Reading, MA: Addison-Wesley, 1992.
[4] T. L. Vincent, "Control using chaos," *IEEE Control Syst. Mag.*, vol. 17, no. 6, pp. 65–76, Dec. 1997.
[5] M. Buehler, D. E. Koditschek, and P. J. Kindlmann, "A simple juggling robot: Theory and experimentation," in *Proc. 1st Int. Symp. Exp. Robot.*, 1990, pp. 35–73.
[6] M. Buehler, D. E. Koditschek, and P. J. Kindlmann, "A family of robot control strategies for intermittent dynamical environments," in *Proc. IEEE Int. Conf. Robot. Autom.*, 1989, pp. 1296–1301.
[7] A. A. Rizzi and D. E. Koditschek, "Further progress in robot juggling: solvable mirror laws," in *Proc. IEEE Int. Conf. Robot. Autom.*, 1994, pp. 2935–2940.
[8] S. Schaal and C. G. Atkeson, "Open loop stable control strategies for robot juggling," in *Proc. IEEE Int. Conf. Robot. Autom.*, 1993, pp. 913–918.
[9] S. Schaal, D. Sternad, and C. G. Atkeson, "One-handed juggling: A dynamical approach to a rhythmic movement task," *J. Motor Behav.*, vol. 28, pp. 165–183, 1996.
[10] G. Baetz, M. Sobotka, D. Wollherr, and M. Buss, "Robot basketball: Ball dribbling—A modified juggling task," in *Advances in Robotics Research*. New York: Springer-Verlag, 2009.
[11] R. P. Ringrose, "Self-stabilizing running," Ph.D. dissertation, Dept. Elect. Eng. Comput. Sci., Mass. Inst. Technol., Cambridge, MA, 2008.
[12] R. R. Burridge, A. A. Rizzi, and D. E. Koditschek, "Sequential composition of dynamically dexterous robot behaviors," *Int. J. Robot. Res.*, vol. 18, no. 6, pp. 534–555, 1998.
[13] A. A. Rizzi and D. E. Koditschek, "Further progress in robot juggling: The spatial two-juggle," in *Proc. IEEE Int. Conf. Robot. Autom.*, 1993, pp. 919–924.
[14] P. Kulchenko and E. Todorov, "First-exit model predictive control of fast discontinuous dynamics: Application to ball bouncing," in *Proc. IEEE Int. Conf. Robot. Autom.*, 2011, pp. 2144–2151.
[15] R. G. Sanfelice, A. R. Teel, and R. Sepulchre, "A hybrid systems approach to trajectory tracking control for juggling systems," in *Proc. IEEE Conf. Decis. Control*, 2007, pp. 5282–5287.
[16] A. Zavala-Rio and B. Brogliato, "On the control of a one degree-of-freedom juggling robot," *Dyn. Control*, vol. 9, no. 1, pp. 67–90, 1999.
[17] S. Schaal and C. G. Atkeson, "Robot juggling: Implementation of memory-based learning," *IEEE Control Syst. Mag.*, vol. 14, no. 1, pp. 57–71, Feb. 1994.
[18] T. Sakaguchi, M. Fujita, H. Watanabe, and F. Miyazaki, "Motion planning and control for a robot performer," in *Proc. IEEE Int. Conf. Robot. Autom.*, 1993, pp. 925–931.
[19] R. Ronsse, P. Lefevre, and R. Sepulchre, "Timing feedback control of a rhythmic system," in *Proc. IEEE Conf. Decis. Control Eur. Control Conf.*, 2005, pp. 6146–6151.
[20] R. Ronsse, P. Lefevre, and R. Sepulchre, "Sensorless stabilization of bounce juggling," *IEEE Trans. Robot.*, vol. 22, no. 1, pp. 147–159, Feb. 2006.
[21] R. Ronsse and R. Sepulchre, "Feedback control of impact dynamics: The bouncing ball revisited," in *Proc. IEEE Conf. Decis. Control*, 2006, pp. 4807–4812.
[22] R. Ronsse, P. Lefevre, and R. Sepulchre, "Rhythmic feedback control of a blind planar juggler," *IEEE Trans. Robot.*, vol. 23, no. 4, pp. 790–802, Aug. 2007.
[23] D. Hobbelen and M. Wisse, "Swing-leg retraction for limit cycle walkers improves disturbance rejection," *IEEE Trans. Robot.*, vol. 24, no. 2, pp. 377–389, Apr. 2008.
[24] D. Hobbelen and M. Wisse, "A disturbance rejection measure for limit cycle walkers: The gait sensitivity norm," *IEEE Trans. Robot.*, vol. 23, no. 6, 1213–1224, Dec. 2007.
[25] K. D. Mombaur, H. G. Bock, J. P. Schloder, and R. W. Longman, "Open-loop stability—a new paradigm for periodic optimal control and analysis of walking mechanisms," in *Proc. IEEE Int. Conf. Robot., Autom. Mechatron.*, 2004, pp. 704–709.
[26] R. Cross, "Grip-slip behavior of a bouncing ball," *Amer. J. Phys.*, vol. 70, no. 11, pp. 1093–1102, 2002.
[27] S. H. Strogatz, *Nonlinear Dynamics and Chaos*, 1st ed. New York: Perseus, 1994.
[28] G. Strang, *Linear Algebra and Its Applications*. Reading, MA: Addison-Wesley, 1988.
[29] LinMot Website. (Jul. 2012). [Online]. Available: www.linmot.com
[30] D-Space Website. (Jul. 2012). [Online]. Available: www.dspace.de
[31] S. Skogestad and I. Postlethwaite, *Multivariable Feedback Control*. New York: Wiley, 2007.
[32] P. Reist and R. D'Andrea, "Design of the Pendulum Juggler," in *Proc. IEEE Int. Conf. Robot. Autom.*, 2011, pp. 5154–5159.

Philipp Reist (S'09) received the B.Sc. and M.Sc. degrees in mechanical engineering from ETH Zurich, Switzerland, in 2007 and 2008, respectively, where, since 2009, he has been working toward the Ph.D. degree with the Institute for Dynamic Systems and Control.

During his studies, he was part of the ETH team that won the Atlanta RoboCup Nanogram tournament and spent two semesters with the Massachusetts Institute of Technology, Cambridge, where he was involved in research on underwater rangefinders and randomized feedback motion planning. His research interests include the control of dynamical systems, nonlinear dynamics, and mechanism design. In addition to research, he regularly teaches robotics workshops for high school students.

Mr. Reist received the Outstanding D-MAVT Bachelor Award for his B.Sc. GPA.

Raffaello D'Andrea (F'10) received the B.Sc. degree in engineering science from the University of Toronto, Toronto, ON, Canada, in 1991 and the M.S. and Ph.D. degrees in electrical engineering from the California Institute of Technology, Pasadena, in 1992 and 1997, respectively.

He was an Assistant Professor, and then an Associate Professor, with Cornell University, Ithaca, NY, from 1997 to 2007. While on leave from Cornell University, from 2003 to 2007, he cofounded Kiva Systems, Woburn, MA, where he led the systems architecture, robot design, robot navigation and coordination, and control algorithms efforts. A creator of dynamic sculpture, his work has appeared at various international venues, including the National Gallery of Canada, the Venice Biennale, Ars Electronica, the Smithsonian, the FRAC Centre, and the Spoleto Festival. He is currently a Professor of dynamic systems and control with ETH Zurich, Zurich, Switzerland, and a Chief Technical Advisor with Kiva Systems.